

TiO₂ surface hybridisation with noble metals (Ag and Cu_xO) for solar de-NO_x and VOC removal

DM Tobaldi,^{a*} L Lajaunie,^{b,‡} MP Seabra,^a R Arenal,^{b,c} JA Labrincha^a

^a *Department of Materials and Ceramics Engineering and CICECO–Aveiro Institute of Materials, University of Aveiro, Campus Universitário de Santiago, 3810-193 Aveiro, Portugal*

^c *Laboratorio de Microscopías Avanzadas, Instituto de Nanociencia de Aragón, Universidad de Zaragoza, 50018 Zaragoza, Spain*

^d *ARAID Foundation, 50018 Zaragoza, Spain*

[‡] *Present address: Departamento de Ciencia de los Materiales e Ingeniería Metalúrgica y Química Inorgánica, Facultad de Ciencias, Universidad de Cádiz, Campus Río San Pedro S/N, Puerto Real 11510, Cádiz, Spain*

Abstract

Indoor and outdoor air pollution remains a major health risk for human beings. Nitrogen oxides and volatile organic compounds are amongst the major pollutant found outdoor. Thus, actions to diminish such risks and to provide safer outdoor / indoor environment are required. In this research work, we have decorated the surface of TiO₂ with noble-metal oxides (Ag and/or Cu_xO) to improve the photocatalytic performances (removal of nitrogen oxides and benzene) under simulated solar-light irradiation. By means of advanced X-ray methods it has been shown that noble metals did not enter the TiO₂ crystal structure, although they retarded the anatase-to-rutile phase transition and crystal growth.

Photocatalytic activity was assessed in the gas-solid phase, monitoring the degradation of NO_x and benzene, using a lamp simulating the solar radiation. Results showed that TiO₂ modified with an Ag:Cu molar ratio equal to 1:1 (with Ag+Cu = 0.5+0.5 mol% = 1 mol%), was that exhibiting best de-NO_x and benzene removal performances.

KEYWORDS: titania; noble-metals surface modification; electron paramagnetic resonance; solar-light

*Corresponding author. Tel.: +351 234 370 041

E-mail addresses: david.tobaldi@ua.pt; david@davidtobaldi.org (DM Tobaldi)

1. Introduction

The rise of cities was the most defining and lasting feature of the Industrial Revolution; this led to the phenomenon called “urbanisation”. Although cities occupy just the 2% of the land in the Earth, they do account for 60–80% of energy consumption and 75% of carbon emissions [1]. An ongoing deterioration of the quality of the air we breathe is a direct consequence of urbanisation. This is considered a significant determinant for our health and well-being, thus air pollution remains a major health risk. In particular, long-term exposure to outdoor air pollution [inorganic, *i.e.* NO_x , a mixture of nitric oxide (NO) and nitrogen dioxide (NO_2), or organic, *i.e.* volatile organic compounds (VOCs), yet the infamous $\text{PM}_{2.5}$, that is a cocktail of chemicals (hydrocarbons, salts and other compounds given off by vehicles, cooking stoves and industry) and other natural components like dust and microorganisms [2]] in urban areas has serious health effects [3] and it is also a key factor in the degradation of surfaces of historical buildings and monuments [4]. Indeed, the World Health Organisation estimated that 9 out of 10 people worldwide breathe air containing high levels of pollutants, this regrettably leading to global mortality related to air pollution [5]. Therefore, it was estimated that each year approximately 7 million deaths can be attributed to outdoor air pollution worldwide [6]. Besides, the composition of VOCs in urban air has a changing face [7]: it has been showed by McDonald *et al.* that there was an “evolution” in air pollution [8]. Those authors demonstrated that the relative importance of chemicals in products like pesticides, coatings, printing inks, adhesives, cleaning agents and personal care products has increased over the years [8]. Furthermore, photochemical smog is a central issue to be aware of: high concentrations of noxious ground-level ozone (O_3) are formed by photochemical reaction amid NO_x and VOCs [9,10]. This is reported to help the formation of secondary organic aerosols from aromatic hydrocarbons, especially in urbanised areas [11], thus having a negative impact on both human health and climate [12,13].

Since the discovery of the Honda-Fujishima effect in 1972 [14], TiO_2 -based photocatalysis (PC) has been regarded as one of the most promising method to combat indoor and outdoor pollution. As well known, TiO_2 's Achilles heel is its wide band gap, limiting its potentiality to the UVA region of the solar spectrum [15]. Surface modification of TiO_2 with noble metal(s) to make noble-metal/metal-oxide nano-hybrids is currently gaining momentum [16]. This is because metallic nanoparticles (NPs) are characterised by their

strong interaction with resonant photons through an excitation of surface plasmon resonance (SPR) [17]. This improves TiO_2 PC activity increasing the photo-reactivity under UVA irradiation as well as enabling absorption in a broad range of visible light [18–21]. Indeed, the junction amid the plasmonic metal and the semiconductor has been shown to give a synergetic optical and electronic effect for unique photoreduction performances under both UV- and visible-light irradiation [22].

In this work we have modified the surface of TiO_2 with silver and/or copper to enhance solar-light induced PC activity. Silver has been chosen because of its well-known properties in enhancing TiO_2 PC activity with both UVA and visible-light sources [23,24], and antibiotic character [25]. On the other hand, copper was selected as it is able to induce visible-light absorption in titania, it has antimicrobial properties [26], yet because of it is relatively inexpensive compared to other noble metals. Still, in the literature there very few works investigating the solar-light PC activity of silver/copper supported on TiO_2 NPs [27,28]. PC results have shown that the optimum Ag:Cu molar ratio for NO_x abatement and benzene removal was 1:1. Furthermore, electron paramagnetic resonance (EPR) spectroscopy, allowed us to identify radical intermediates that were formed upon UVA or visible-light exposure, thus giving accurate information about reaction pathways in the reacting system.

2. Experimental section

2.1 Sample preparation

A modified aqueous sol-gel method was used for the synthesis of TiO_2 -based photocatalysts; a detailed procedure can be found elsewhere [29]. To do the Ag/Cu modified TiO_2 , stoichiometric amounts of silver(I) nitrate (Sigma-Aldrich, $\geq 99.0\%$) and copper(II) nitrate trihydrate (Sigma-Aldrich, $\geq 98.5\%$) were added to the TiO_2 -based sol when this had a 1 M concentration. Two series of modified specimens were synthesised: one with Ag+Cu = 1 mol%, with Cu mol% = 0, 0.25, 0.50, 0.75, 1.00 mol%. The other having Ag+Cu = 2 mol%, with Cu mol% = 0, 0.50, 1.00, 1.50, 2.00 mol%. Afterwards, dried gels were thermally treated at 450 °C under a static air flow, using an electric muffle furnace. The heating/cooling rate was 5 °C min⁻¹, with a 2 h dwell time at the selected temperature. Samples were referred to as **Ti450** (unmodified TiO_2), **Agx/Cuy** in case of Ag/Cu modified TiO_2 , where x stands for the Ag mol%, and y for the Cu mol% (*i.e.* TiO_2 modified with 0.75 mol% Ag and 0.25 mol% Cu has been labelled: **Ag0.75/Cu0.25**). The end members were labelled to as **Ag-TiO₂** and **Cu-TiO₂** in case of 1 mol%; **2Ag-TiO₂** and **2Cu-TiO₂** in case of 2 mol%.

2.2 Sample characterisation

The size distributions of the starting sols were measured through dynamic light scattering (DLS), using a Zetasizer Nano ZS (Malvern Instruments, UK). Four drops of the 1 M sol were added to a cuvette of Milli-Q water, dispersed ultrasonically for 10 min, and measured at room temperature. The scattering was measured at an angle of 173°, using a laser emitting at 633 nm, and the refractive indexes of water and the $\text{Ti}(\text{OH})_4$ based sol particles were assumed to be 1.33 and 2.50, respectively [30]. Reported results are averaged over three consecutive measurements (each measurement comprised 15 runs).

X-ray powder diffraction (XRPD) was used to quantify the crystalline fraction of the prepared specimens. For this purpose, XRPD patterns for semi-quantitative phase analysis (QPA) were recorded at room temperature on a θ/θ diffractometer (PANalytical X'Pert Pro, NL), equipped with a fast RTMS detector (PIXcel 1D, PANalytical), with $\text{Cu K}\alpha$ radiation (45 kV and 40 mA, 20–80 °2 θ range, with a virtual step scan of 0.02 °2 θ , and virtual time per step of 200 s). The Rietveld data analysis for obtaining QPA information was assessed using the GSAS software package [31], and its graphical interface EXPGUI [32]. Instrumental broadening, obtained from the refinement of LaB_6 standard (NIST SRM 660b), was taken into account in all of the Rietveld refinements. These latter were accomplished by refining the following parameters: scale-factors, zero-point, 6 coefficients of the shifted Chebyshev function to fit the background, unit cell parameters. The profile was modelled using the Thompson-Cox-Hasting formulation of the pseudo-Voigt function [33], and two Lorentzian (L_x and L_y) terms, peak correction for asymmetry, as well as sample displacement effects, were refined. The Gaussian parameter (G_w , that is an angle independent term) of the pseudo-Voigt profile shape function of the phases constituting the samples was instead constrained to the value obtained for LaB_6 (NIST SRM 660b). The starting atomic parameters for anatase, rutile and brookite, described in the space groups (SGs) $I4_1/amd$, $P4_2/mnm$ and $Pbca$, respectively, were taken from the literature [34–36]. Microstructural features of the specimens were determined *via* XRPD too, using the same instrument and setup as per the QPA, but in the 20–145 °2 θ range, with a virtual step-scan of 0.1 °2 θ , and virtual time per step of 500 s, aiming to handle data with a higher signal-to-noise ratio. The whole powder pattern modelling (WPPM) [37,38], as implemented in the PM2K software [39], was used for the microstructural analysis of the diffraction data. Diffracting domains are nanocrystalline, thus they were assumed to be strain free and their shape was approximated to be spherical, with diameter distributed according to a log-normal curve (*i.e.* strain contributions to the peak profile were neglected, and peak broadening was assumed isotropic). The instrumental contribution was obtained by parametrising the profile of 18 hkl reflections from the NIST SRM 660b standard (LaB_6), according to the Caglioti *et al.* relationship [40]. To assess the WPPM modelling we used the anatase (SG $I4_1/amd$), rutile (SG $P4_2/mnm$) and brookite (SG $Pbca$) phases; then we refined those parameters: background (that was modelled using a 6th-order Chebyshev polynomial), peak intensities, specimen displacement, unit cell parameters, mean and variance of the log-normal size distributions.

High-resolution scanning transmission electron microscopy (HR-STEM) experiments were performed using an FEI Titan low-base microscope operated at 300 kV and equipped with a CESCOR Cs probe corrector, an ultrabright X-FEG electron source and a monochromator. HR-STEM imaging was performed using high-angle annular dark field (HAADF) and annular bright field (ABF) detectors. Automatic indexation of the FFT patterns was performed by using the JEMS software [41]. Spatially-resolved electron energy loss spectroscopy experiments were also performed with a monochromated beam (energy resolution of 210 meV with a dispersion of 0.03 eV per pixel). For TEM studies, samples were dispersed in ethanol in an ultrasound bath for a few minutes and a drop of the suspension was placed onto a molybdenum/nickel grids coated with carbon membrane.

The apparent optical energy band-gap (E_g) was evaluated by means of optical spectroscopy. Diffuse reflectance (DR) spectra were recorded on a Shimadzu UV-3100 spectrometer (JP), equipped with an integrating sphere and a white reference material made of Spectralon®; the UV-Vis spectral range (250–850 nm) was investigated, with 0.2 nm in resolution. The Tauc formalism was adopted to extract the E_g of the specimens [42], according to an indirect transition [43]. To this end, DR data were transformed into pseudo-absorption spectra $F(R)=\alpha$ according to the Kubelka-Munk theory: $F(R)=\alpha=(1-R)^2/2R$, where R is the reflectance [44]. Afterwards, the Tauc method was applied: $\alpha h\nu=\alpha_0(h\nu-E_g)^\gamma$, where α_0 is a constant and the power coefficient γ for an indirect transition is equal to 2.

2.2 Functional applications

2.3.1 Photocatalytic activity: gas-solid phase

PC activity experiments were assessed in the gas–solid phase, monitoring the degradation of NO_x gases and benzene (C₆H₆), as they are known to be amongst the most harmful pollutants negatively influencing air quality in urban environments [45], both indoor and outdoor. All of the gas-solid phase PC studies were carried out in a reactor that operated continuously [46]. The condition of continuous flow was necessary to achieve sample saturation, ensuring that, during the test, the PC process was the only one involved (*i.e.*, no absorption from the sample nor from the reactor walls) [47]. It comprised a cylindrical chamber (3.8 L internal volume) built from a high grade stainless steel with a stainless steel top with a sealed glass window to allow the light to reach the sample that was placed inside. The light source employed was a light imitating the solar spectrum [Osram Ultra-Vitalux, 300 W, its emission spectrum being showed in Figure S1, (supplementary information file)]. This was positioned 33 cm above the photocatalyst; the light intensity reaching the surface of the photocatalyst was then equal to 3.5 mW.cm⁻² in the UV-A range, and 35 mW.cm⁻² in the visible spectral range. [It has to be stressed here that the radiant flux (in the UV-A and visible regions) entering the reactor is significantly lower compared to that of xenon arc lamps, that are frequently used in the catalytic community (*i.e.* in the order of around 8 mW.cm⁻² in the UV-A region, and

80 m.W cm⁻² in the visible, see for instance references [48–50]).] A Petri dish 6 cm in diameter was filled up with a layer of powder. The tests were assessed at 24±1 °C (temperature inside the reactor) with a relative humidity of 36%. These parameters – stable throughout the tests – were controlled by means of a thermocouple that was placed inside the chamber, and a humidity sensor placed in the inlet pipe. As per the de-NO_x PC experiments, the initial concentration of NO_x (prepared using synthetic air and NO_x gas) was set at 200 ppb [It has to be noted that such concentration is higher than that commonly reported outdoor, *e.g.* outdoor urban levels have an annual mean range of 20–90 µg.m⁻³ (around 11–48 ppb) [3]]. The outlet concentration of NO_x gases was measured using a chemiluminescence analyser (AC-30 M, Environment SA, FR), according to a procedure that we described in very detail previously [21,51].

When benzene was used as model gas, its concentration exiting through the outlet was measured using a VOC-72M gas analyser (Environment SA, FR), that is based on gas chromatography and photo-ionisation detector. The inlet gas mixture (prepared mixing gas cylinders containing synthetic air and C₆H₆) was allowed to flow into the chamber until it stabilised at a concentration of ~260 µg.m⁻³ (~80 ppb). This concentration was chosen because the World Health Organisation recommends an exposure to total VOCs < 300 µg.m⁻³ during 8 h/day [52]. The mixture of air with that concentration of C₆H₆ was guaranteed using two mass flow controllers with a flow rate of 150 mL.min⁻¹.

The experiments were conducted by placing the Petri dish containing the photocatalyst inside the reactor and covering the glass window. Once the desired NO_x/C₆H₆ concentration was reached and attained stable level into the reactor, the window glass was uncovered, the lamp turned on and the PC reaction started. PC tests were all repeated in triplicate to check recyclability and photo-stability of the photocatalysts [53]. PC data are presented as formal quantum efficiency (FQE) values which is defined as the molecules degraded over incident photons [54]. The total irradiation time for FQE determination was set at 10 min for the de-NO_x experiments, and 6 h for the removal of benzene. It is important to stress that FQE reflects the lowest estimate of the true quantum efficiency [55]. Therefore, aiming to have a better comparison between the tested specimens, data relative to the first 2 min (de-NO_x) or 60 min (C₆H₆ removal) of reaction time, were interpreted according to a first order kinetic law.

3. Results and discussion

3.1 QPA and Microstructural Analyses: XRPD and HR-STEM

DLS results are listed in Table S1. Particles dispersed in the unmodified titanium sol had a number average diameter of 4.8 nm, and a polydispersity index (PDI) of 0.343, thus the particles in the sols are “moderately” polydisperse. Addition of Ag and Cu salts to the Ti sol did not lead to any considerable variation in the average diameter of the particles dispersed in the sol, see Table S1. However, a general increase in the PDI happened, this being > 0.4 in the Ag/Cu modified TiO₂, meaning highly polydisperse values [56].

XRPD QPA results are listed in Table 1; a graphical output of a Rietveld QPA refinement is shown in Figure S2 (**Ag1/Cu1**). Unmodified TiO₂ specimen (**Ti450**) was composed of the three TiO₂ polymorphs: anatase (56.5 wt%), rutile (19.8 wt%) and brookite (23.6 wt%) – anatase is the thermodynamically stable TiO₂ polymorph on the nanoscale [57], yet brookite is a common “by-product” of the synthesis when precipitation is carried out in acidic medium [58]. Modification with silver (1 and 2 mol%) retarded the anatase-to-rutile phase transition (ART). Indeed, **Ag-TiO₂** had 83.7 wt% anatase, 5.4 wt% rutile and 10.9 wt% brookite; **2Ag-TiO₂** had a very close mineralogy, being composed of 83.0 wt% anatase, 4.5 wt% rutile and 12.5 wt% brookite.

Table 1 – Rietveld agreement factors and quantitative phase composition of the unmodified and Ag/Cu-modified TiO₂.*

Sample	No. of variables	Agreement factors			Phase composition (wt%)		
		$R(F^2)$ (%)	R_{wp} (%)	χ^2	anatase	rutile	brookite
Ti450[‡]	20	3.54	4.03	1.74	56.5±0.1	19.8±0.2	23.6±0.6
Ag-TiO₂	19	5.56	4.55	2.01	83.7±0.1	5.4±0.3	10.9±0.4
Ag0.75/Cu0.25	21	3.77	3.24	1.44	91.6±0.1	5.3±0.4	3.1±0.2
Ag0.50/Cu0.50	20	3.71	3.58	1.46	94.9±0.1	3.9±0.3	1.2±0.2
Ag0.25/Cu0.75[†]	19	2.27	3.01	1.59	94.5±0.1	4.4±0.2	1.2±0.2
Cu-TiO₂[‡]	20	3.16	3.60	2.03	82.2±0.1	9.0±0.2	8.8±0.8
2Ag-TiO₂	19	4.32	3.96	1.79	83.0±0.1	4.5±0.3	12.5±0.4
Ag1.50/Cu0.50	20	2.30	2.84	1.56	74.6±0.1	5.8±0.2	19.6±0.4
Ag1/Cu1	21	3.51	2.82	1.54	77.9±0.1	5.4±0.2	16.7±0.3
Ag0.50/Cu1.50[†]	18	2.04	3.48	1.56	93.4±0.1	4.8±0.2	1.8±0.2
2Cu-TiO₂[‡]	22	4.44	3.74	2.07	81.4±0.1	8.8±0.2	9.8±0.8

* There were 2285 observations for every refinement; the number of anatase, rutile and brookite reflections was 32, 31 and 155, respectively. [†]From [59]; [‡]from [26].

Copper modification led to very close results: ART was hindered (though in lesser extent compared to Ag modification), as **Cu-TiO₂** was composed of 82.2 wt% anatase, 9.0 wt% rutile and 8.8 wt% brookite. **2Cu-TiO₂** composition was similar, anatase accounting for 81.4 wt%, rutile being 8.8 wt%, brookite being the remaining wt%, *cf* Table 1. Double (Ag+Cu = 1 mol%) TiO₂ modification retarded even more the ART. For instance, anatase was present in wt% ranging from 91.6 to 94.5 w% in **Ag0.75/Cu0.25** and **Ag0.25/Cu0.75**, respectively. A different scenario appeared when the Ag+Cu modification was equal to 2 mol%. ART was indeed retarded compared to **Ti450**, but to a lesser extent in comparison with **2Ag-TiO₂** or **2Cu-TiO₂**. As a matter of fact, with molar amounts of silver equal to 1.50 and 1.00 mol% (this meaning: copper molar amounts = 0.50 and 1.00 mol%, respectively), brookite crystallisation was favoured at the expenses of anatase. **Ag1.50/Cu0.50** was made of 74.6 wt% anatase, 5.8w% rutile and 19.6wt% brookite. Similarly, an equimolar amount of Ag and Cu (**Ag1/Cu1**) resulted in 77.9 wt% anatase, 5.4 wt% rutile and 16.7 wt% brookite. Switching the molar amount of copper to 1.50 mol% (**Ag0.50/Cu1.50**), favoured a stabilisation of the anatase TiO₂ polymorph (this being 93.4 wt%), consistent with recent literature [60]. Generally speaking, modification of TiO₂ with Ag+Cu retarded the ART in each case. ART is known to be a nucleation-growth mechanism [61], thus introducing silver and copper in the TiO₂ system led to a grain-boundary pinning (*i.e.* Zener pinning) [59], which eventually culminates in delaying the ART. This is also reflected by a decrease in the mean average diameter of the crystalline domains, see WPPM microstructural information reported in Tables 2–4 – an example of WPPM graphical output is shown in Figure S3. Anatase crystalline domains in unmodified TiO₂ have an average diameter of 10.4 nm, those of rutile of 14.4 nm. Silver and copper modification of TiO₂ led not only to smaller crystalline domain diameters, but also to narrower size distribution of those crystalline domains, as shown in Table 2. Addition of silver and silver and copper had a greater effect in decreasing the average size of both anatase and rutile diameters. For instance, anatase in **Ag-TiO₂** had an average diameter equal to 6.0 nm; that of rutile was 11.5 nm. Anatase in the Ag+Cu equimolar specimen (**Ag0.50/Cu0.50**) had and average diameter of 5.1 nm, rutile of 12.8 nm. Copper addition had a minor effect in decreasing the size of the coherently scattering domains: 8.0 nm and 12.1 nm were the diameters of anatase and rutile, respectively, in **Cu-TiO₂**. Double amount of silver and/or copper led to a more pronounced reduction of the crystalline domains of both anatase and rutile. The double modification had a greater effect in the decrease of rutile average diameters (see Table 2, third column). Furthermore, looking at the virtually nil differences in unit cell volumes (Table 3), neither Ag nor Cu entered the TiO₂ structure. Indeed, the ionic radii of ^[VI]Ag^{1+/2+}, ^[VI]Cu^{1+/2+} and ^[VI]Ti⁴⁺ are 1.15/0.94, 0.77/0.73 and 0.61 Å, respectively [62]. However, the very slight changes in tetragonality (*cf* Table 4), might suggest the presence of some local structure distortion in both anatase and rutile (in the Ag+Cu modified specimens).

Table 2 – Mean crystalline domain size of anatase (ant) and rutile (rt) – defined as the mean of the lognormal size distributions; maximum values (mode), median, skewness of the lognormal size distributions, and dispersity index (\mathcal{D}), as derived from the WPPM method. The apparent optical E_g of the samples, according to an indirect transition, are listed in the last column.

Sample	Mean crystalline domain diameter		Mode of the size distribution		Median of the size distribution		Skewness of the size distribution		\mathcal{D}		Indirect E_g^*	
	$\langle D_{\text{ant}} \rangle$ (nm)	$\langle D_{\text{rt}} \rangle$ (nm)	Ant (nm)	Rt (nm)	Ant (nm)	Rt (nm)	Ant (nm)	Rt (nm)	Ant	Rt	eV	nm
Ti450[‡]	10.4±0.7	14.4±0.6	9.4±0.6	9.9±0.4	10.0±0.6	12.7±0.5	0.8±0.1	1.8±0.1	0.07±0.01	0.29±0.04	2.94	422
Ag-TiO₂	6.0±0.6	11.5±2.5	5.1±0.9	8.1±1.8	5.6±0.6	10.2±2.2	1.1±0.1	1.7±0.1	0.12±0.05	0.26±0.15	2.79	444
Ag0.75/Cu0.25	5.6±0.6	11.6±3.7	4.4±0.5	10.1±3.2	5.1±0.6	11.0±3.5	1.3±0.1	0.9±0.1	0.18±0.03	0.09±0.07	2.73	454
Ag0.50/Cu0.50	5.1±0.5	12.8±5.3	3.8±0.4	8.8±3.6	4.6±0.5	11.3±4.6	1.5±0.1	1.8±0.1	0.21±0.03	0.28±0.04	2.71	458
Ag0.25/Cu0.75[†]	6.7±0.3	11.2±0.1	5.3±0.2	9.4±0.1	6.2±0.2	10.6±0.2	1.3±0.1	1.1±0.1	0.16±0.09	0.13±0.02	2.81	442
Cu-TiO₂[‡]	8.0±0.2	12.1	6.6±0.2	8.5±0.8	7.5±0.2	10.7±0.9	1.1±0.1	1.7±0.1	0.13±0.06	0.26±0.06	2.79	444
2Ag-TiO₂	5.4±1.4	10.4±1.8	4.6±1.2	8.5±1.5	5.1±1.3	9.7±1.7	1.1±0.1	1.2±0.1	0.12±0.04	0.15±0.06	2.70	459
Ag1.50/Cu0.50	5.8±0.3	6.6±0.6	4.9±0.3	4.4±0.6	5.5±0.3	5.8±0.6	1.1±0.1	1.8±0.1	0.12±0.08	0.30±0.04	2.65	468
Ag1/Cu1	5.6±0.5	7.7±1.0	4.7±0.4	4.9±0.6	5.3±0.4	6.6±0.9	1.1±0.1	2.0±0.1	0.12±0.01	0.35±0.08	2.55	486
Ag0.50/Cu1.50[†]	5.2±0.8	9.4±0.3	4.0±0.1	8.2±0.3	4.7±0.3	9.0±0.8	1.4±0.1	0.9±0.1	0.20±0.01	0.09±0.07	2.75	452
2Cu-TiO₂[‡]	8.8±0.2	10.3±0.9	7.9±0.2	6.8±0.6	8.4±0.2	9.0±0.8	0.8±0.1	1.9±0.1	0.07±0.03	0.32±0.07	2.75	451

[†]From [59]; [‡]from [26]; * the relative errors in the E_g estimations were < 1%.

Table 3 – WPPM agreement factors and unit cell parameters for the anatase, rutile and brookite TiO₂ polymorphs in the synthesised Ag/Cu-TiO₂ specimens.

Sample	Agreement factors			Unit cell parameters									
	R_{wp} (%)	R_{exp} (%)	χ^2	Anatase			Rutile			Brookite			
				$a=b$ (nm)	c (nm)	V (nm ³)	$a=b$ (nm)	c (nm)	V (nm ³)	a (nm)	b (nm)	c (nm)	V (nm ³)
Ti450[†]	6.17	1.96	3.15	0.3791(1)	0.9515(1)	0.137(1)	0.4598(1)	0.2959(1)	0.063(1)	0.5440(2)	0.9206(4)	0.5157 (1)	0.258(1)
Ag-TiO₂	3.63	2.52	1.44	0.3787(4)	0.9503(12)	0.136(2)	0.4594(3)	0.2959(2)	0.062(1)	0.5455(19)	0.9134(18)	0.5164(9)	0.257(4)
Ag0.75/Cu0.25	3.55	2.57	1.38	0.3791(2)	0.9510(6)	0.137(1)	0.4601(5)	0.2935(6)	0.062(3)	0.5467(35)	0.9110(18)	0.5156(7)	0.257(7)
Ag0.50/Cu0.50	3.48	2.61	1.33	0.3790(2)	0.9510(6)	0.137(1)	0.4599(3)	0.2947(3)	0.062(1)				–
Ag0.25/Cu0.75[†]	2.83	2.04	1.39	0.3790(1)	0.9516(2)	0.137(1)	0.4608(1)	0.2955(1)	0.063(1)				–
Cu-TiO₂[‡]	2.53	2.09	1.21	0.3790(1)	0.9510(3)	0.137(1)	0.4600(1)	0.2959(1)	0.063(1)	0.5459(4)	0.9129(29)	0.5147(7)	0.256(2)
2Ag-TiO₂	2.83	2.43	1.16	0.3788(4)	0.9487(16)	0.136(2)	0.4599(5)	0.2959(4)	0.063(2)	0.5485(55)	0.9156(75)	0.5171(23)	0.260(14)
Ag1.50/Cu0.50	3.03	1.94	1.56	0.3793(1)	0.9524(9)	0.137(1)	0.4606(3)	0.2956(3)	0.063(1)	0.5470(17)	0.9185(22)	0.5171(5)	0.260(4)
Ag1/Cu1	3.04	1.95	1.56	0.3794(1)	0.9516(10)	0.137(1)	0.4607(2)	0.2958(2)	0.063(1)	0.547825	0.9167(24)	0.5186(8)	0.260(5)
Ag0.50/Cu1.50[†]	3.56	1.88	1.89	0.3790(2)	0.9514(4)	0.137(1)	0.4596(3)	0.2959(4)	0.062(1)				–
2Cu-TiO₂[‡]	3.85	1.95	1.97	0.3790(1)	0.9511(3)	0.137(1)	0.4600(1)	0.2961(1)	0.063(1)	0.5455(6)	0.9105(37)	0.5144(6)	0.255(2)

[†]From [59]; [‡]from [26].

Table 4 – Tetragonality (c/a) in anatase and rutile TiO_2 polymorphs.

Sample	Tetragonality (c/a)	
	Anatase	Rutile
Ti450	2.5099(3)	0.6435(4)
Ag-TiO₂	2.5094(16)	0.6441(9)
Ag0.75/Cu0.25	2.5086(8)	0.6379(23)
Ag0.50/Cu0.50	2.5092(8)	0.6408(12)
Ag0.25/Cu0.75	2.5108(3)	0.6413(4)
Cu-TiO₂	2.5092(4)	0.6433(4)
2Ag-TiO₂	2.5045(20)	0.6434(17)
Ag1.50/Cu0.50	2.5109(10)	0.6418(12)
Ag1/Cu1	2.5082(11)	0.6421(8)
Ag0.50/Cu1.50	2.5103(7)	0.6438(15)
2Cu-TiO₂	2.5095(4)	0.6437(4)

HR-STEM imaging was performed to confirm these findings. HR-STEM images acquired on the sample **Ti450** are shown in Figure 1. The diameter of the grains is between 4 nm and 60 nm and the high-crystalline quality of them can be appreciated in Figure 1b. However, for this sample, indexation of the FFT patterns is ambiguous because the same pattern can be ascribed to either anatase or rutile phases. To get more information on this point, EELS analyses were performed in the energy range corresponding to the $\text{Ti-L}_{2,3}$ edges (Figure 1c). The EELS spectra show chemical inhomogeneity which corresponds to a mixed phases [63]. In particular EELS fine structures corresponding to a mix of anatase, rutile and/or brookite phases can be clearly highlighted. This confirms the results obtained by XPRD. STEM HAADF images of **Ag0.50/Cu1.50** are shown in Figure 2. The presence of nanoparticles which are dispersed in the TiO_2 matrix and with a diameter situated between 5 and 10 nm can be seen in Figure 2a. They have a brighter contrast than the surrounding matrix which highlights a higher atomic number. The crystalline nature of these nanoparticles is highlighted in Figure 2b and the automatic indexation of the FFT pattern by using the JEMS software [41], showed that these nanoparticles correspond to the Ag face-centred cubic structure described in the [011] zone axis.

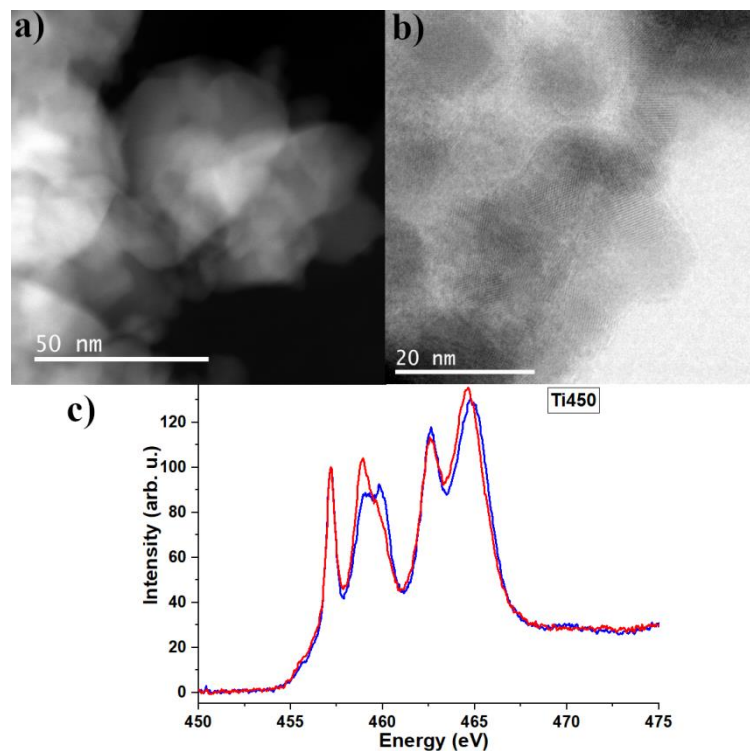


Figure 1 – a) HR-STEEM HAADF micrograph of the sample **Ti450**; b) HR-STEM ABF micrograph of **Ti450**; c) EELS spectra acquired on the sample **Ti450** and showing the Ti-L_{2,3} edges.

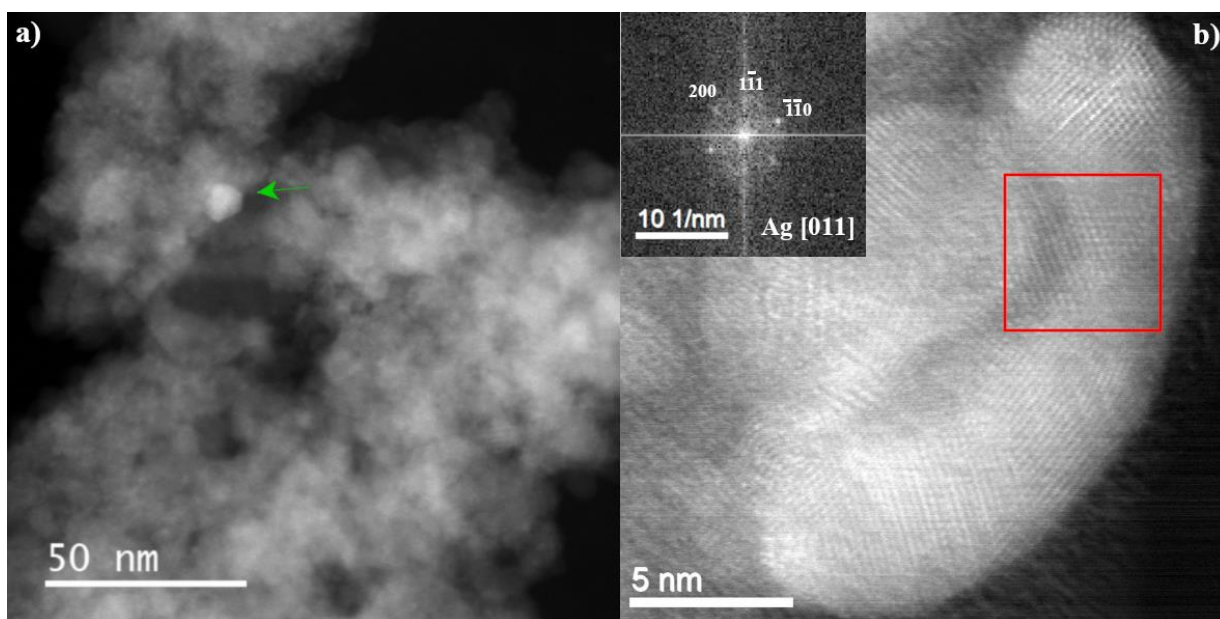


Figure 2 – a) STEEM HAADF micrograph of the sample **Ag0.50/Cu1.50**. The green arrow highlights the presence of nanoparticles with a brighter contrast than the surrounding matrix b) HR-STEM HAADF micrograph of the sample **Ag0.50/Cu1.50**. The inset displays the FFT pattern obtained on the area highlighted by the red square.

3.2 Optical properties: DRS

DR spectra are shown in Figure 3. The absorption band located at < 3.0 eV is ascribed to the band gap transition in TiO_2 [44]; the absorption feature in **2Ag-TiO₂** and **Ag1/Cu1**, located at around 2.75 eV, belongs to interfacial charge transfer (IFCT), that is the electron transferring from the valence band of TiO_2 to the Ag and/or Cu_xO clusters that are grafted around titania [64]. The weak band at approximately 2.25 eV in **2Ag-TiO₂** can be tentatively attributed to the localised SPR in Ag^0 [65], or to the uphill electron transfer process from Ag^0 to the conduction band of TiO_2 – plasmon-induced charge separation (PICS) [66]. The strong absorption band seen at lower energies (< 2.25 eV) and centred at ~ 1.5 eV in **Ag1/Cu1** and **2Cu-TiO₂**, belongs to $d-d$ electronic transition in Cu^{2+} [67].

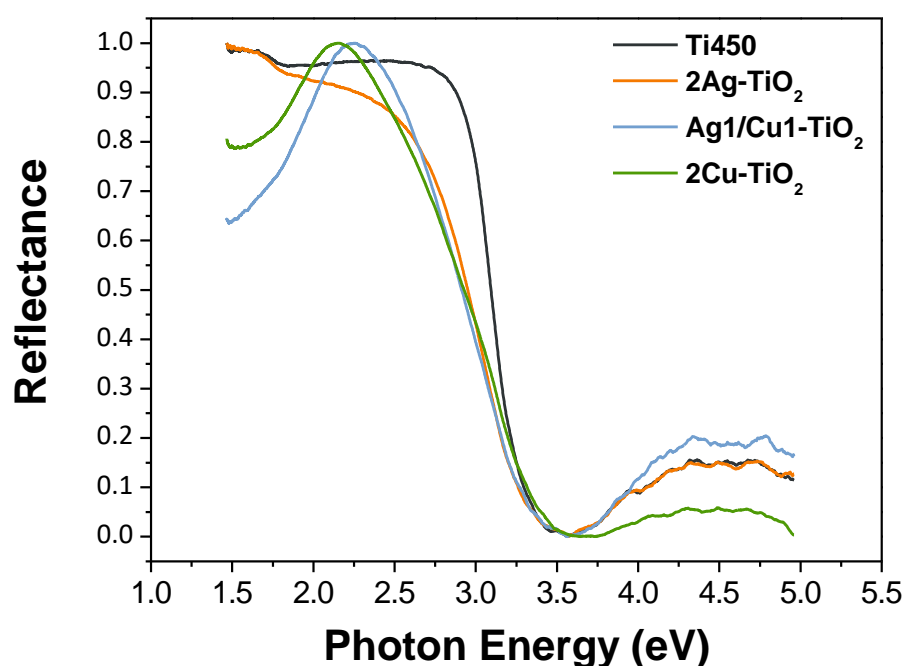


Figure 3 – Diffuse reflectance spectra of selected specimens. Reflectance values on the y-axis are normalised.

The apparent optical E_g was estimated *via* the Tauc formalism, taking into account an indirect transition (Figure S4, **Ag1.5/Cu0.5**). The obtained values are listed in Table 2 (12th and 13th columns). **Ti450** had an indirect E_g equal to 2.94. This is consistent with the expected value for rutile, as this TiO_2 polymorph possesses a stronger relative response factor for diffuse reflectance than that of anatase [68] – that specimen contained 19.8 wt% rutile, see Table 1. Addition of Ag/Cu systematically shifted the apparent optical E_g toward lower energies, this meaning that those specimens can (potentially) harvest visible-light. However, it has to be stressed that E_g values reported in Table 2 do not necessarily correspond to an actual upward shift of the valence band edge toward the conduction band of TiO_2 , or to a real contraction of the actual band-gap [69].

3.4 Functional properties

In this section are only discussed the de-NO_x results and C₆H₆ removal tests of specimens in which Ag+Cu = 1 mol%. Previous literature showed that an excessive loading of both Cu and Ag to be detrimental for the PC activity: both CuO/Ag likely behaved as recombination centres (see for instance Figure S5) [70–72].

3.4.1 Gas-solid phase photocatalytic activity: de-NO_x

Results describing the de-NO_x PC activity, over 10 min irradiation time, are shown in Figure 4a-c. Unmodified TiO₂ displayed a de-NO_x rate of 2.5×10^{-3} molecules.photon⁻¹. As per the mono-modified TiO₂ specimens, they both were more active than **Ti450**, with **Ag-TiO₂** being more active than **Cu-TiO₂**, having a NO_x removal rate of 3.9×10^{-3} , and 2.6×10^{-3} molecules.photon⁻¹, respectively (Figure 4b). Those results are somehow confirmed by the kinetic constant (k'_{app}) for the initial 2 min of reaction time, Figure 4c. **Ti450** had a k'_{app} value of 6.9×10^{-2} min⁻¹, being followed by **Cu-TiO₂** (7.8×10^{-2} min⁻¹), and **Ag-TiO₂** being the most active (8.9×10^{-2} min⁻¹). This is quite expected for **Ag-TiO₂**, as when a noble-metal/metal-oxide nano-hybrids system is irradiated with UV-light, electrons in the semiconductor are promoted from the valence band to the conduction band. They are then transferred to the Fermi level of the noble-metal, thus favouring the separation of e⁻/h⁺ photo-generated pair [21], as depicted in Scheme 1a. On the other hand, from DR measurements, we know that copper was (mostly) in its cupric form. CuO valence band and conduction band are sandwiched between those of TiO₂ [73], as shown in Scheme 1b. This scenario, that is: type-I band alignment, favours a charge recombination [60]: a charge transfer from both the conduction band and valence band of TiO₂ to those of CuO happens. This agrees well with previous literature in which copper modification of TiO₂ has been reported to not improve the PC performances of titania, because of the afore-mentioned charge recombination [60,74,75]. As per the Ag/Cu modified specimens, **Ag0.50/Cu0.50** was the most active sample, as also shown by the FQE rate (4.2×10^{-3} molecules.photon⁻¹) and the initial (first 2 min of reaction) pseudo-first order kinetic constants (12.5×10^{-2} min⁻¹), cf Figure 4b,c. According to Remita *et al.* [28], when Ag and CuO are grafted on TiO₂ NPs, they scavenge electrons, thus inducing an increase in the PC activity – Ag NPs act themselves as an electron trap for both TiO₂ and CuO. However, according to those authors, an Ag:Cu = 1:3 ratio was found to be the optimum for phenol degradation [28]; yet, Ovcharov *et al.* reported the molar ratio Ag:Cu=1:6 to be the optimum for PC carbon dioxide reduction [27].

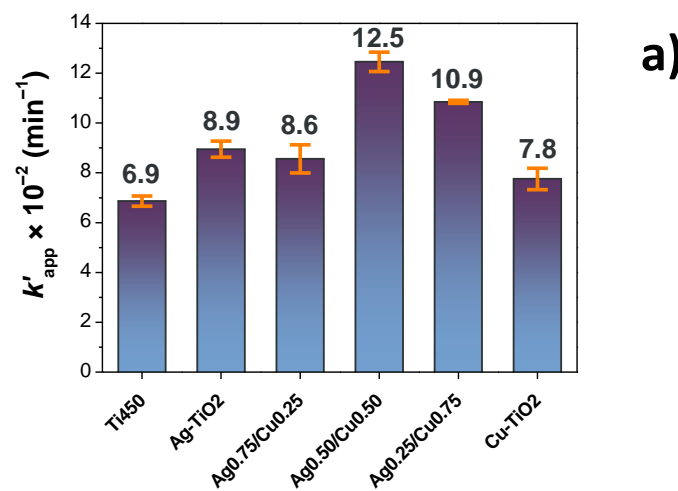
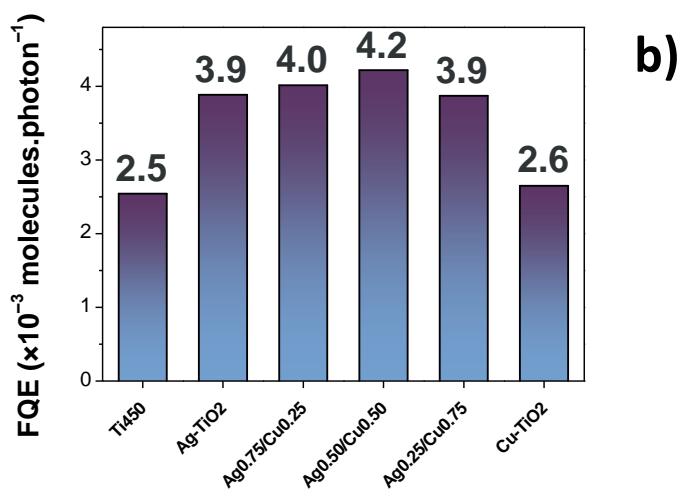
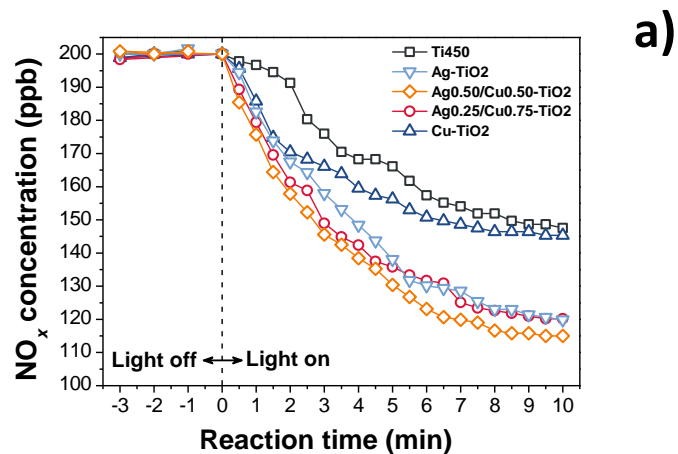


Figure 4 – a) NO_x degradation graph of selected samples irradiated with the solar lamp. The initial negative time zone indicates a period of stabilisation of the chamber; positive time indicates that the light has been turned on, starting the experiment; b) FQEs values for NO_x abatement over 10 min reaction time; c) photocatalytic de-NO_x reported as the pseudo-first-order kinetic constant (k'_{app}) for the initial 2 min of reaction time. Error bars are the standard error.

Still, such an efficient charge separation is able to increase the lifetime of the photo-generated exciton, thus improving the PC activity, *cf* Scheme 1c, in which the left side is supposed to dominate. Moreover, the visible component present in the solar lamp is able to sensitise TiO₂ by transferring excited electrons from CuO/Ag NPs to the conduction band of TiO₂ through IFCT [24,76], thus further enhancing the PC activity. Therefore, those PC redox reactions are proposed to happen in the Ag/Cu-modified TiO₂ specimens:



Equations (1) to (3) depict the typical PC reactions at the surface of a semiconductor material, that are the charge carrier (exciton) generation [*i.e.* Equation (1)], as well as the trapping of an e⁻ and of a h⁺ to give active hydroxyls and oxygen radicals, see Equations (2) and (3). Equations (4) to (8) describe the oxidation reactions by oxygen radicals and hydroxyl radicals – with Equations (4) and (5) being more likely to happen in **Ag0.50/Cu0.50**, as shown in Figure 5, in which is reported a plot of the degradation of NO and NO₂ *versus* reaction time of **Ag0.50/Cu0.50**. In it, it is shown that the concentration of NO₂, after having turned the lamp on, is virtually stable, whilst that of NO is degraded. Therefore, as suggested by recent literature, O₂^{•-} should be the main active oxidative species for the PC reduction of NO [51]. As a final point, nitric acid is the end-product of NO_x PC degradation [77], however it can be easily eluted from the catalyst into water, thus the de-NO_x cycle should be closed *via* Equation (9) [78].

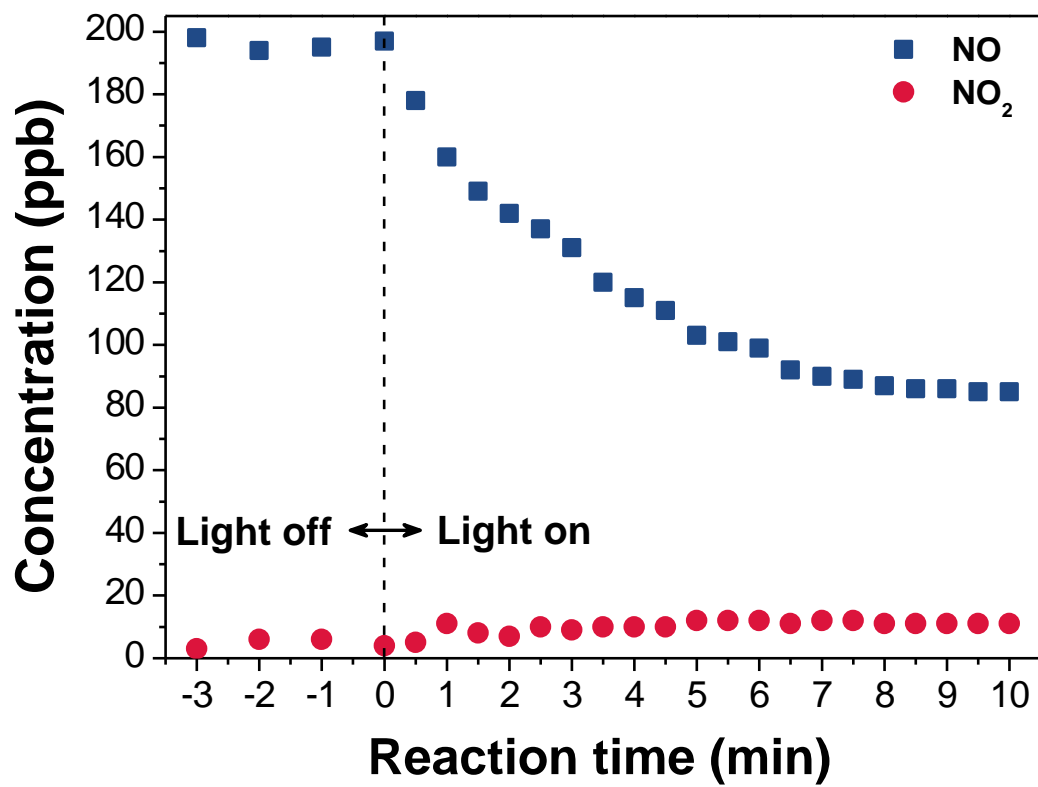
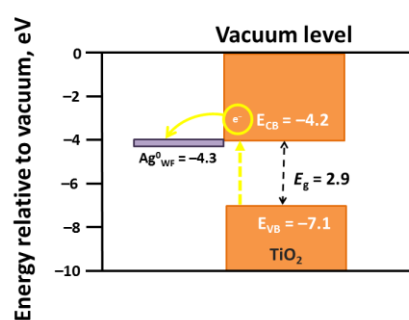


Figure 5 – Concentration of NO and NO₂ versus irradiation time, specimen Ag0.50/Cu0.50.

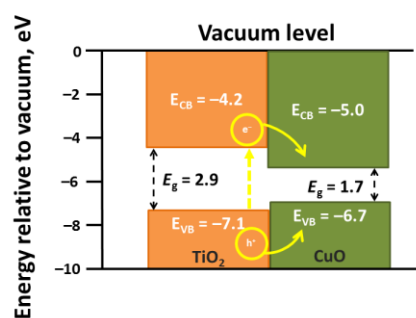
Potential Vs AVS

Scheme 1a



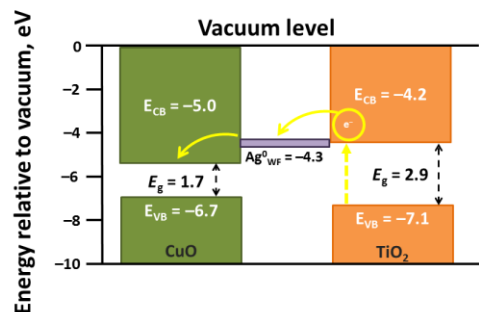
Potential Vs AVS

Scheme 1b



Potential Vs AVS

Scheme 1c



Scheme 1 – Proposed band alignment relative to the absolute vacuum scale (AVS) in: a) an anatase– Ag^0 system; b) an anatase– CuO system; c) an anatase– Ag^0 – CuO system. The energy levels of TiO_2 are from specimen **Ti450** (this work); those of CuO from Xu and Schoonen [79]; the value of the work function (WF) in Ag^0 is from Michaelson [80].

Note that, although the data reported here might not reflect a rigorous picture of the absolute values of conduction band and valence band potentials, they provide a reasonable estimate of the relative band edge positions.

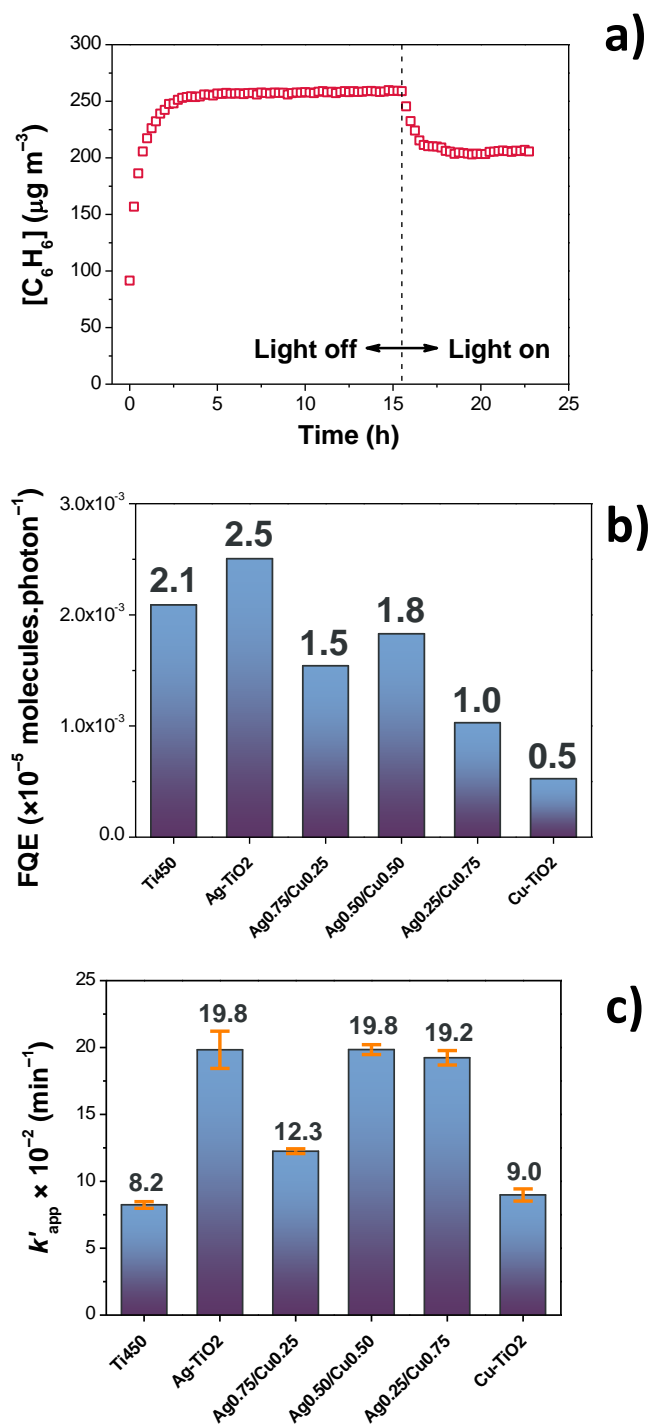


Figure 6 – a) Benzene removal graph of specimen **Ag0.25/Cu0.75**. b) FQEs rates for benzene removal over 6 h reaction time; c) benzene removal reported as the pseudo-first-order kinetic constant (k'_{app}) for the initial 60 min of reaction time. The error bars represent the standard error.

3.4.2 Gas-solid phase photocatalytic activity: benzene removal

An example of benzene removal plot is shown in Figure 6a, whilst in Figure 6b,c are depicted the benzene removal data, reported as FQE rates over 6 h irradiation time, and as the initial (first 60 min of reaction) pseudo-first order kinetic constants, k'_{app} . **Ti450** showed a removal rate of benzene of 2.1×10^{-3} molecules.photon⁻¹. **Ag-TiO₂** was the best performing specimen in terms of FQE benzene removal rate (2.5×10^{-5} molecules.photon⁻¹). Still, over 6 h irradiation time, Ag/Cu specimens had FQE rate lower than that of unmodified TiO₂ (Figure 6b). Again, the less active TiO₂ specimen in benzene removal was that modified with 1 mol% copper (FQE = 0.5×10^{-5} molecules.photon⁻¹), confirming itself to be not a good candidate to improve TiO₂ solar PC activity. However, considering the initial kinetic of benzene removal (first 1 h irradiation), Figure 6c, the best performing specimens were **Ag-TiO₂**, **Ag0.50/Cu0.50**, and **Ag0.25/Cu0.75** (19.8×10^{-2} , 19.8×10^{-2} , and 19.2×10^{-2} min, respectively), which is in a way a trend close to that obtained with the abatement of NO_x gases.

PC oxidation of benzene is quite a complex matter. According to Einaga and co-workers, the highly reactive [•]OH radical [see Equation (2)] can oxidise benzene to CO₂ [81]. These authors stated that, during benzene oxidation, many kinds of intermediate radicals might be formed, including cyclohexadienyl radical, which in turn can be subsequently oxidised to a hydroperoxyl radical. These intermediate radicals are eventually decomposed to CO₂ and CO, and/or transformed to other intermediate species [81]. Otherwise, Ollis *et al.*, proposed benzene degradation to follow two routes: (I) direct h⁺ oxidation to yield phenol; (II) benzene polymerisation – benzene radical cation might react with an incoming benzene molecule, or a benzene molecule adsorbed on the surface, to form polymers [82]. Han *et al.*, identified 11 gaseous by-products from the PC oxidation of benzene – these were all saturated hydrocarbons, less toxic than benzene [83]. Or else, recently, Selishchev and colleagues found that the conversion of benzene led to the formation of CO as a harmful by-product (approximately 5%) [84]. Yet, Lyulyukin *et al.*, by means of FT-IR spectroscopy, reported that benzene is completely (photocatalytically) oxidised to CO₂ and CO without the formation of any gaseous intermediates [85]. As it is seen, benzene PC degradation is quite an intricate matter, with still no utter consensus amongst the scientific community about the intermediates compounds formed during its (photo)-oxidation. Indeed, from the gas-chromatograms available in this work, we could mainly detect the formation of intermediates compounds that are lighter than benzene (Figure S6), probably alkanes and/or alkenes and/or alkynes [more investigation is needed to clarify this complex point]. Indeed, **Ti450** was found to be yellowish after the benzene removal reaction. The FT-IR band (Figure S7) appearing at around 1430 cm⁻¹ was tentatively assigned to some aromatic compounds [87]. A similar behaviour has been observed by Ollis *et al.* [82]. However, likewise those authors, specimens were regenerated and recovered in a pure air flow and under UVA-irradiation, the specimens being reusable. Besides, as suggested by Lichtin and Sadeghi [86], the formation of those intermediates might inhibit the reaction(s)

responsible for the removal of benzene, thus initiating a competition amid benzene and those degradation products (and among degradation products themselves) that can interfere in the kinetic of benzene removal. A complete VOC degradation is therefore a staggeringly intricate matter: for instance, Jenkin and colleagues have detected 1,926 different degradation steps together with the formation of 602 unique intermediate organic species before CO and water were finally formed in the isoprene (C₅H₈) atmospheric oxidation [88].

Conclusions

Hybrid Ag/Cu-TiO₂ composite semiconductive materials were synthesised by means of an aqueous sol-gel method. The photocatalytic activity of prepared materials was tested by monitoring the abatement of NO_x and the removal of a volatile organic compound (benzene) in the gas-solid phase. An excessive loading of both Cu and Ag (> 1 mol%) showed itself to be detrimental for photocatalytic activity. Addition of silver and copper (**Ag0.50/Cu0.50**) greatly increased titania's ability in the photocatalytic removal of NO_x. This was shown to be due to an efficient charge separation that grants an increase in the lifetime of the photo-generated exciton. On the other hand, hybridisation of TiO₂ with 1 mol% Ag (**Ag-TiO₂**) proved itself to be the optimum in the photocatalytic removal of benzene, although its photocatalytic oxidation confirmed to be a complicated issue. Modification of TiO₂ with copper was unfavourable for titania solar induced photocatalytic activity. This work demonstrated that the judicious choice (or exclusion) and amount of modifying agents is essential for granting the optimum efficiency in TiO₂ solar induced removal of pollutants in the gas-solid phase.

Acknowledgements

This work was developed within the scope of the bilateral project between Portugal and Slovakia, FCT/484/15/01/2019/S and within the scope of the project CICECO-Aveiro Institute of Materials, UIDB/50011/2020 & UIDP/50011/2020, financed by national funds through the Portuguese Foundation for Science and Technology/MCTES. David Maria Tobaldi, although *“not so young”* and/or *“not having given a sufficient level of relevance and impact on the scientific community considering his age”*, is very much grateful to FCT and to Portuguese national funds (OE), through FCT, I.P., in the scope of the framework contract foreseen in the numbers 4, 5 and 6 of the article 23, of the Decree-Law 57/2016, of August 29, changed by Law 57/2017, of July 19. The STEM measurements were performed in the Laboratorio de Microscopias Avanzadas (LMA) at the Instituto de Nanociencia de Aragon (INA)—Universidad de Zaragoza (Spain). Raul Arenal gratefully acknowledges the support from the Spanish Ministerio de Economia y

Competitividad (MAT2016-79776-P), from the Government of Aragon, and the European Social Fund under the project “Construyendo Europa desde Aragon” 2014–2020 (grant number E/26). Lastly, but not less importantly, we are very much obliged to Miss Dafne Maria Glaglanon for proof-editing the English of the manuscript.

References

- [1] H. Akbari, C. Cartalis, D. Kolokotsa, A. Muscio, A.L. Pisello, F. Rossi, M. Santamouris, A. Synnef, N.H. Wong, M. Zinzi, Local climate change and urban heat island mitigation techniques – the state of the art, *J. Civ. Eng. Manag.* 22 (2016) 1–16. <https://doi.org/10.3846/13923730.2015.1111934>.
- [2] X. Li, L. Jin, H. Kan, Air pollution: a global problem needs local fixes, *Nature*. 570 (2019) 437. <https://doi.org/10.1038/d41586-019-01960-7>.
- [3] W.H.O.R.O. for Europe, Air quality guidelines for Europe, (2000). <https://apps.who.int/iris/handle/10665/107335> (accessed February 12, 2019).
- [4] F. Di Turo, C. Proietti, A. Screpanti, M.F. Fornasier, I. Cionni, G. Favero, A. De Marco, Impacts of air pollution on cultural heritage corrosion at European level: What has been achieved and what are the future scenarios, *Environ. Pollut.* 218 (2016) 586–594. <https://doi.org/10.1016/j.envpol.2016.07.042>.
- [5] WHO | Mortality and burden of disease from ambient air pollution, WHO. (n.d.). http://www.who.int/gho/phe/outdoor_air_pollution/burden/en/ (accessed June 28, 2019).
- [6] WHO | Air pollution, WHO. (n.d.). <http://www.who.int/airpollution/en/> (accessed February 12, 2019).
- [7] A.C. Lewis, The changing face of urban air pollution, *Science*. 359 (2018) 744–745. <https://doi.org/10.1126/science.aar4925>.
- [8] B.C. McDonald, J.A. de Gouw, J.B. Gilman, S.H. Jathar, A. Akherati, C.D. Cappa, J.L. Jimenez, J. Lee-Taylor, P.L. Hayes, S.A. McKeen, Y.Y. Cui, S.-W. Kim, D.R. Gentner, G. Isaacman-VanWertz, A.H. Goldstein, R.A. Harley, G.J. Frost, J.M. Roberts, T.B. Ryerson, M. Trainer, Volatile chemical products emerging as largest petrochemical source of urban organic emissions, *Science*. 359 (2018) 760–764. <https://doi.org/10.1126/science.aag0524>.
- [9] M.D. Shaw, J.D. Lee, B. Davison, A. Vaughan, R.M. Purvis, A. Harvey, A.C. Lewis, C.N. Hewitt, Airborne determination of the temporo-spatial distribution of benzene, toluene, nitrogen oxides and ozone in the boundary layer across Greater London, UK, *Atmospheric Chem. Phys.* 15 (2015) 5083–5097. <https://doi.org/10.5194/acp-15-5083-2015>.
- [10] X. Fang, M. Shao, A. Stohl, Q. Zhang, J. Zheng, H. Guo, C. Wang, M. Wang, J. Ou, R.L. Thompson, R.G. Prinn, Top-down estimates of benzene and toluene emissions in the Pearl River Delta and Hong Kong, China, *Atmospheric Chem. Phys.* 16 (2016) 3369–3382. <https://doi.org/10.5194/acp-16-3369-2016>.
- [11] D.K. Henze, J.H. Seinfeld, N.L. Ng, J.H. Kroll, T.-M. Fu, D.J. Jacob, C.L. Heald, Global modeling of secondary organic aerosol formation from aromatic hydrocarbons: high- vs. low-yield pathways, *Atmospheric Chem. Phys.* 8 (2008) 2405–2420. <https://doi.org/10.5194/acp-8-2405-2008>.
- [12] M. Shiraiwa, K. Ueda, A. Pozzer, G. Lammel, C.J. Kampf, A. Fushimi, S. Enami, A.M. Arangio, J. Fröhlich-Nowoisky, Y. Fujitani, A. Furuyama, P.S.J. Lakey, J. Lelieveld, K. Lucas, Y. Morino, U. Pöschl, S. Takahama, A. Takami, H. Tong, B. Weber, A. Yoshino, K. Sato, Aerosol Health Effects from Molecular to Global Scales, *Environ. Sci. Technol.* 51 (2017) 13545–13567. <https://doi.org/10.1021/acs.est.7b04417>.
- [13] K. Tsigaridis, M. Kanakidou, The Present and Future of Secondary Organic Aerosol Direct Forcing on Climate, *Curr. Clim. Change Rep.* 4 (2018) 84–98. <https://doi.org/10.1007/s40641-018-0092-3>.
- [14] A. Fujishima, K. Honda, Electrochemical Photolysis of Water at a Semiconductor Electrode, *Nature*. 238 (1972) 37–38. <https://doi.org/10.1038/238037a0>.
- [15] A. Fujishima, X. Zhang, D. Tryk, TiO₂ photocatalysis and related surface phenomena, *Surf. Sci. Rep.* 63 (2008) 515–582. <https://doi.org/10.1016/j.surfrep.2008.10.001>.

- [16] X. Liu, J. Iocozzia, Y. Wang, X. Cui, Y. Chen, S. Zhao, Z. Li, Z. Lin, Noble metal–metal oxide nanohybrids with tailored nanostructures for efficient solar energy conversion, photocatalysis and environmental remediation, *Energy Environ. Sci.* 10 (2017) 402–434. <https://doi.org/10.1039/C6EE02265K>.
- [17] S. Linic, P. Christopher, D.B. Ingram, Plasmonic-metal nanostructures for efficient conversion of solar to chemical energy, *Nat. Mater.* 10 (2011) 911–921. <https://doi.org/10.1038/nmat3151>.
- [18] X. Zhang, Y.L. Chen, R.-S. Liu, D.P. Tsai, Plasmonic photocatalysis, *Rep. Prog. Phys.* 76 (2013) 046401. <https://doi.org/10.1088/0034-4885/76/4/046401>.
- [19] S. Banerjee, S.C. Pillai, P. Falaras, K.E. O'Shea, J.A. Byrne, D.D. Dionysiou, New Insights into the Mechanism of Visible Light Photocatalysis, *J. Phys. Chem. Lett.* 5 (2014) 2543–2554. <https://doi.org/10.1021/jz501030x>.
- [20] S. Linic, U. Aslam, C. Boerigter, M. Morabito, Photochemical transformations on plasmonic metal nanoparticles, *Nat. Mater.* 14 (2015) 567–576. <https://doi.org/10.1038/nmat4281>.
- [21] M. Karmaoui, L. Lajaunie, D.M. Tobaldi, G. Leonardi, C. Benbayer, R. Arenal, J.A. Labrincha, G. Neri, Modification of anatase using noble-metals (Au, Pt, Ag): Toward a nanoheterojunction exhibiting simultaneously photocatalytic activity and plasmonic gas sensing, *Appl. Catal. B Environ.* 218 (2017) 370–384. <https://doi.org/10.1016/j.apcatb.2017.06.010>.
- [22] L. Collado, A. Reynal, F. Fresno, M. Barawi, C. Escudero, V. Perez-Dieste, J.M. Coronado, D.P. Serrano, J.R. Durrant, V.A. de la P. O'Shea, Unravelling the effect of charge dynamics at the plasmonic metal/semiconductor interface for CO₂ photoreduction, *Nat. Commun.* 9 (2018) 4986. <https://doi.org/10.1038/s41467-018-07397-2>.
- [23] M.K. Seery, R. George, P. Floris, S.C. Pillai, Silver doped titanium dioxide nanomaterials for enhanced visible light photocatalysis, *J. Photochem. Photobiol. Chem.* 189 (2007) 258–263. <https://doi.org/10.1016/j.jphotochem.2007.02.010>.
- [24] D.M. Tobaldi, M.J. Hortigüela Gallo, G. Otero-Irurueta, M.K. Singh, R.C. Pullar, M.P. Seabra, J.A. Labrincha, Purely Visible-Light-Induced Photochromism in Ag–TiO₂ Nanoheterostructures, *Langmuir*. 33 (2017) 4890–4902. <https://doi.org/10.1021/acs.langmuir.6b04474>.
- [25] A.B.G. Lansdown, Silver in healthcare : its antimicrobial efficacy and safety in use, Royal Society of Chemistry, Cambridge, 2010.
- [26] D.M. Tobaldi, N. Rozman, M. Leoni, M.P. Seabra, A.S. Škapin, R.C. Pullar, J.A. Labrincha, Cu–TiO₂ Hybrid Nanoparticles Exhibiting Tunable Photochromic Behavior, *J. Phys. Chem. C*. 119 (2015) 23658–23668. <https://doi.org/10.1021/acs.jpcc.5b07160>.
- [27] M.L. Ovcharov, V.V. Shvalagin, V.M. Granchak, Photocatalytic Reduction of CO₂ on Mesoporous TiO₂ Modified with Ag/Cu Bimetallic Nanostructures, *Theor. Exp. Chem.* 50 (2014) 175–180. <https://doi.org/10.1007/s11237-014-9362-x>.
- [28] M.G. Méndez-Medrano, E. Kowalska, A. Lehoux, A. Herissan, B. Ohtani, D. Bahena, V. Briois, C. Colbeau-Justin, J.L. Rodríguez-López, H. Remita, Surface Modification of TiO₂ with Ag Nanoparticles and CuO Nanoclusters for Application in Photocatalysis, *J. Phys. Chem. C*. 120 (2016) 5143–5154. <https://doi.org/10.1021/acs.jpcc.5b10703>.
- [29] D.M. Tobaldi, R.C. Pullar, A.F. Gualtieri, M.P. Seabra, J.A. Labrincha, Sol–gel synthesis, characterisation and photocatalytic activity of pure, W-, Ag- and W/Ag co-doped TiO₂ nanopowders, *Chem. Eng. J.* 214 (2013) 364–375. <https://doi.org/10.1016/j.cej.2012.11.018>.
- [30] D.M. Tobaldi, R.C. Pullar, R. Binions, A. Belen Jorge, P.F. McMillan, M. Saeli, M.P. Seabra, J.A. Labrincha, Influence of sol counter-ions on the visible light induced photocatalytic behaviour of TiO₂ nanoparticles, *Catal. Sci. Technol.* 4 (2014) 2134. <https://doi.org/10.1039/c4cy00423j>.
- [31] A.C. Larson, R.B. Von Dreele, General Structure Analysis System (GSAS), Los Alamos National Laboratory Report LAUR, 2004.
- [32] B.H. Toby, EXPGUI, a graphical user interface for GSAS, *J. Appl. Crystallogr.* 34 (2001) 210–213. <https://doi.org/10.1107/S0021889801002242>.
- [33] P. Thompson, D.E. Cox, J.B. Hastings, Rietveld refinement of Debye–Scherrer synchrotron X-ray data from Al₂O₃, *J. Appl. Crystallogr.* 20 (1987) 79–83. <https://doi.org/10.1107/S0021889887087090>.
- [34] C.J. Howard, T.M. Sabine, F. Dickson, Structural and thermal parameters for rutile and anatase, *Acta Crystallogr. B*. 47 (1991) 462–468. <https://doi.org/10.1107/S010876819100335X>.

- [35] E.P. Meagher, G.A. Lager, Polyhedral thermal expansion in the TiO₂ polymorphs; refinement of the crystal structures of rutile and brookite at high temperature, *Can Miner.* 17 (1979) 77–85.
- [36] D.M. Tobaldi, R.C. Pullar, A.F. Gualtieri, M.P. Seabra, J.A. Labrincha, Phase composition, crystal structure and microstructure of silver and tungsten doped TiO₂ nanopowders with tuneable photochromic behaviour, *Acta Mater.* 61 (2013) 5571–5585. <https://doi.org/10.1016/j.actamat.2013.05.041>.
- [37] P. Scardi, M. Leoni, Whole powder pattern modelling, *Acta Crystallogr. A* 58 (2002) 190–200. <https://doi.org/10.1107/S0108767301021298>.
- [38] P. Scardi, M. Leoni, Whole Powder Pattern Modelling: Theory and Applications, in: *Diffraction Analysis of Microstructures*, Springer-Verlag, Eric J. Mittemeijer, Paolo Scardi, Berlin, 2004: pp. 51–92.
- [39] M. Leoni, T. Confente, P. Scardi, PM2K: a flexible program implementing Whole Powder Pattern Modelling, *Z. Für Krist. Suppl.* 23 (2006) 249–254. https://doi.org/10.1524/zksu.2006.suppl_23.249.
- [40] G. Caglioti, A. Paoletti, F.P. Ricci, On resolution and luminosity of a neutron diffraction spectrometer for single crystal analysis, *Nucl. Instrum. Methods* 9 (1960) 195–198. [https://doi.org/10.1016/0029-554X\(60\)90101-4](https://doi.org/10.1016/0029-554X(60)90101-4).
- [41] P. Stadelmann, JEMS-SAAS, (2014).
- [42] A. Dolgonos, T.O. Mason, K.R. Poeppelmeier, Direct optical band gap measurement in polycrystalline semiconductors: A critical look at the Tauc method, *J. Solid State Chem.* 240 (2016) 43–48. <https://doi.org/10.1016/j.jssc.2016.05.010>.
- [43] T. Zhu, S.-P. Gao, The Stability, Electronic Structure, and Optical Property of TiO₂ Polymorphs, *J. Phys. Chem. C* 118 (2014) 11385–11396. <https://doi.org/10.1021/jp412462m>.
- [44] R.G. Burns, *Mineralogical Applications of Crystal Field Theory*, Cambridge University Press, 1993.
- [45] R.M. Harrison, R.E. Hester, eds., *Air Quality in Urban Environments*, Royal Society of Chemistry, Cambridge, 2009. <http://ebook.rsc.org/?DOI=10.1039/9781847559654> (accessed January 6, 2015).
- [46] D.M. Tobaldi, L. Lajaunie, M. López Haro, R.A.S. Ferreira, M. Leoni, M.P. Seabra, J.J. Calvino, L.D. Carlos, J.A. Labrincha, Synergy of Neodymium and Copper for Fast and Reversible Visible-light Promoted Photochromism, and Photocatalysis, in *Cu/Nd-TiO₂ Nanoparticles*, *ACS Appl. Energy Mater.* 2 (2019) 3237–3252. <https://doi.org/10.1021/acsaem.9b00084>.
- [47] U.I. Gaya, A.H. Abdullah, Heterogeneous photocatalytic degradation of organic contaminants over titanium dioxide: A review of fundamentals, progress and problems, *J. Photochem. Photobiol. C Photochem. Rev.* 9 (2008) 1–12. <https://doi.org/10.1016/j.jphotochemrev.2007.12.003>.
- [48] S. Obregón, G. Colón, Excellent photocatalytic activity of Yb³⁺, Er³⁺ co-doped BiVO₄ photocatalyst, *Appl. Catal. B Environ.* 152–153 (2014) 328–334. <https://doi.org/10.1016/j.apcatb.2014.01.054>.
- [49] H. Wang, X. Gao, G. Duan, X. Yang, X. Liu, Facile preparation of anatase–brookite–rutile mixed-phase N-doped TiO₂ with high visible-light photocatalytic activity, *J. Environ. Chem. Eng.* 3 (2015) 603–608. <https://doi.org/10.1016/j.jece.2015.02.006>.
- [50] L. Da Vià, C. Recchi, E.O. Gonzalez-Yañez, T.E. Davies, J.A. Lopez-Sanchez, Visible light selective photocatalytic conversion of glucose by TiO₂, *Appl. Catal. B Environ.* 202 (2017) 281–288. <https://doi.org/10.1016/j.apcatb.2016.08.035>.
- [51] A. Giampiccolo, D.M. Tobaldi, S.G. Leonardi, B.J. Murdoch, M.P. Seabra, M.P. Ansell, G. Neri, R.J. Ball, Sol gel graphene/TiO₂ nanoparticles for the photocatalytic-assisted sensing and abatement of NO₂, *Appl. Catal. B Environ.* 243 (2019) 183–194. <https://doi.org/10.1016/j.apcatb.2018.10.032>.
- [52] World Health Organization, WHO. Guidelines for Indoor Air Quality: Selected Pollutants, 2010., WHO - Guidel. Indoor Air Qual. Sel. Pollut. (2010). www.euro.who.int/__data/assets/pdf_file/0009/128169/e94535.pdf.
- [53] D.M. Tobaldi, M.P. Seabra, G. Otero-Irurueta, Y.R. de Miguel, R.J. Ball, M.K. Singh, R.C. Pullar, J.A. Labrincha, Quantitative XRD characterisation and gas-phase photocatalytic activity testing for visible-light (indoor applications) of KRONOClean 7000®, *RSC Adv.* 5 (2015) 102911–102918. <https://doi.org/10.1039/C5RA22816F>.
- [54] A. Mills, S. Le Hunte, An overview of semiconductor photocatalysis, *J. Photochem. Photobiol. Chem.* 108 (1997) 1–35. [https://doi.org/10.1016/S1010-6030\(97\)00118-4](https://doi.org/10.1016/S1010-6030(97)00118-4).

- [55] T. Watanabe, T. Takizawa, K. Honda, Photocatalysis through excitation of adsorbates. 1. Highly efficient N-deethylation of rhodamine B adsorbed to cadmium sulfide, *J. Phys. Chem.* 81 (1977) 1845–1851. <https://doi.org/10.1021/j100534a012>.
- [56] S. Bhattacharjee, DLS and zeta potential – What they are and what they are not?, *J. Controlled Release*. 235 (2016) 337–351. <https://doi.org/10.1016/j.jconrel.2016.06.017>.
- [57] H. Zhang, J.F. Banfield, Thermodynamic analysis of phase stability of nanocrystalline titania, *J. Mater. Chem.* 8 (1998) 2073–2076. <https://doi.org/10.1039/a802619j>.
- [58] A. Di Paola, M. Bellardita, L. Palmisano, Brookite, the Least Known TiO₂ Photocatalyst, *Catalysts*. 3 (2013) 36–73. <https://doi.org/10.3390/catal3010036>.
- [59] D.M. Tobaldi, S.G. Leonardi, K. Movlaee, L. Lajaunie, M.P. Seabra, R. Arenal, G. Neri, J.A. Labrincha, Hybrid Noble-Metals/Metal-Oxide Bifunctional Nano-Heterostructure Displaying Outperforming Gas-Sensing and Photochromic Performances, *ACS Omega*. 3 (2018) 9846–9859. <https://doi.org/10.1021/acsomega.8b01508>.
- [60] C. Byrne, L. Moran, D. Hermosilla, N. Merayo, Á. Blanco, S. Rhatigan, S. Hinder, P. Ganguly, M. Nolan, S.C. Pillai, Effect of Cu doping on the anatase-to-rutile phase transition in TiO₂ photocatalysts: Theory and experiments, *Appl. Catal. B Environ.* 246 (2019) 266–276. <https://doi.org/10.1016/j.apcatb.2019.01.058>.
- [61] R.D. Shannon, J.A. Pask, Kinetics of the Anatase-Rutile Transformation, *J. Am. Ceram. Soc.* 48 (1965) 391–398. <https://doi.org/10.1111/j.1151-2916.1965.tb14774.x>.
- [62] R.D. Shannon, Revised effective ionic radii and systematic studies of interatomic distances in halides and chalcogenides, *Acta Crystallogr. Sect. A*. 32 (1976) 751–767. <https://doi.org/10.1107/S0567739476001551>.
- [63] J.P. Crocombette, F. Jollet, Ti 2p X-ray absorption in titanium dioxides (TiO₂): the influence of the cation site environment, *J. Phys. Condens. Matter*. 6 (1994) 10811. <https://doi.org/10.1088/0953-8984/6/49/022>.
- [64] H. Irie, K. Kamiya, T. Shibamura, S. Miura, D.A. Tryk, T. Yokoyama, K. Hashimoto, Visible Light-Sensitive Cu(II)-Grafted TiO₂ Photocatalysts: Activities and X-ray Absorption Fine Structure Analyses, *J. Phys. Chem. C*. 113 (2009) 10761–10766. <https://doi.org/10.1021/jp903063z>.
- [65] K.L. Kelly, E. Coronado, L.L. Zhao, G.C. Schatz, The Optical Properties of Metal Nanoparticles: The Influence of Size, Shape, and Dielectric Environment, *J. Phys. Chem. B*. 107 (2003) 668–677. <https://doi.org/10.1021/jp026731y>.
- [66] T. Tatsuma, H. Nishi, T. Ishida, Plasmon-induced charge separation: chemistry and wide applications, *Chem. Sci.* 8 (2017) 3325–3337. <https://doi.org/10.1039/C7SC00031F>.
- [67] F.C. Hawthorne, Mineralogical Society of America, eds., Spectroscopic methods in mineralogy and geology, Mineralogical Society of America, Washington, D.C., 1988.
- [68] A.M. Pennington, A.I. Okonmah, D.T. Munoz, G. Tsilomelekis, F.E. Celik, Changes in Polymorph Composition in P25-TiO₂ during Pretreatment Analyzed by Differential Diffuse Reflectance Spectral Analysis, *J. Phys. Chem. C*. 122 (2018) 5093–5104. <https://doi.org/10.1021/acs.jpcc.7b10449>.
- [69] F. Spadavecchia, G. Cappelletti, S. Ardizzone, C.L. Bianchi, S. Cappelli, C. Oliva, P. Scardi, M. Leoni, P. Fermo, Solar photoactivity of nano-N-TiO₂ from tertiary amine: role of defects and paramagnetic species, *Appl. Catal. B Environ.* 96 (2010) 314–322. <https://doi.org/10.1016/j.apcatb.2010.02.027>.
- [70] N. Sobana, M. Muruganadham, M. Swaminathan, Nano-Ag particles doped TiO₂ for efficient photodegradation of Direct azo dyes, *J. Mol. Catal. Chem.* 258 (2006) 124–132. <https://doi.org/10.1016/j.molcata.2006.05.013>.
- [71] G. Li, N.M. Dimitrijevic, L. Chen, T. Rajh, K.A. Gray, Role of Surface/Interfacial Cu²⁺ Sites in the Photocatalytic Activity of Coupled CuO–TiO₂ Nanocomposites, *J. Phys. Chem. C*. 112 (2008) 19040–19044. <https://doi.org/10.1021/jp8068392>.
- [72] S.J.A. Moniz, J. Tang, Charge Transfer and Photocatalytic Activity in CuO/TiO₂ Nanoparticle Heterojunctions Synthesised through a Rapid, One-Pot, Microwave Solvothermal Route, *ChemCatChem*. 7 (2015) 1659–1667. <https://doi.org/10.1002/cctc.201500315>.
- [73] D.M. Tobaldi, C. Piccirillo, N. Rozman, R.C. Pullar, M.P. Seabra, A.S. Škapin, P.M. Castro, J.A. Labrincha, Effects of Cu, Zn and Cu-Zn addition on the microstructure and antibacterial and photocatalytic

- functional properties of Cu-Zn modified TiO₂ nano-heterostructures, *J. Photochem. Photobiol. Chem.* 330 (2016) 44–54.
- [74] R. López, R. Gómez, M.E. Llanos, Photophysical and photocatalytic properties of nanosized copper-doped titania sol–gel catalysts, *Catal. Today*. 148 (2009) 103–108. <https://doi.org/10.1016/j.cattod.2009.04.001>.
- [75] G. Colón, M. Maicu, M.C. Hidalgo, J.A. Navío, Cu-doped TiO₂ systems with improved photocatalytic activity, *Appl. Catal. B Environ.* 67 (2006) 41–51. <https://doi.org/10.1016/j.apcatb.2006.03.019>.
- [76] K.K. Mandari, B.S. Kwak, A.K.R. Police, M. Kang, In-situ photo-reduction of silver particles and their SPR effect in enhancing the photocatalytic water splitting of Ag₂O/TiO₂ photocatalysts under solar light irradiation: A case study, *Mater. Res. Bull.* 95 (2017) 515–524. <https://doi.org/10.1016/j.materresbull.2017.08.028>.
- [77] Y. Ohko, Y. Nakamura, A. Fukuda, S. Matsuzawa, K. Takeuchi, Photocatalytic Oxidation of Nitrogen Dioxide with TiO₂ Thin Films under Continuous UV-Light Illumination, *J. Phys. Chem. C*. 112 (2008) 10502–10508. <https://doi.org/10.1021/jp802959c>.
- [78] J.S. Dalton, P.A. Janes, N.G. Jones, J.A. Nicholson, K.R. Hallam, G.C. Allen, Photocatalytic oxidation of NO_x gases using TiO₂: a surface spectroscopic approach, *Environ. Pollut.* 120 (2002) 415–422. [https://doi.org/10.1016/S0269-7491\(02\)00107-0](https://doi.org/10.1016/S0269-7491(02)00107-0).
- [79] Y. Xu, M.A.A. Schoonen, The absolute energy positions of conduction and valence bands of selected semiconducting minerals, *Am. Mineral.* 85 (2000) 543–556.
- [80] H.B. Michaelson, The work function of the elements and its periodicity, *J. Appl. Phys.* 48 (1977) 4729–4733. <https://doi.org/10.1063/1.323539>.
- [81] H. Einaga, T. Ibusuki, S. Futamura, Photocatalytic Oxidation of Benzene in Air, *J. Sol. Energy Eng.* 126 (2004) 789–793. <https://doi.org/10.1115/1.1687402>.
- [82] O. d’Hennezel, P. Pichat, D.F. Ollis, Benzene and toluene gas-phase photocatalytic degradation over H₂O and HCL pretreated TiO₂: by-products and mechanisms, *J. Photochem. Photobiol. Chem.* 118 (1998) 197–204. [https://doi.org/10.1016/S1010-6030\(98\)00366-9](https://doi.org/10.1016/S1010-6030(98)00366-9).
- [83] S.-W. Han, J.-H. Lee, J.-S. Kim, S.-H. Oh, Y.-K. Park, H.-O. Kim, Gaseous by-products from the TiO₂ Photocatalytic Oxidation of Benzene, *Environ. Eng. Res.* 13 (2008) 14–18. <https://doi.org/10.4491/eer.2008.13.1.014>.
- [84] D.S. Selishchev, N.S. Kolobov, A.A. Pershin, D.V. Kozlov, TiO₂ mediated photocatalytic oxidation of volatile organic compounds: Formation of CO as a harmful by-product, *Appl. Catal. B Environ.* 200 (2017) 503–513. <https://doi.org/10.1016/j.apcatb.2016.07.044>.
- [85] M.N. Lyulyukin, P.A. Kolinko, D.S. Selishchev, D.V. Kozlov, Hygienic aspects of TiO₂-mediated photocatalytic oxidation of volatile organic compounds: Air purification analysis using a total hazard index, *Appl. Catal. B Environ.* 220 (2018) 386–396. <https://doi.org/10.1016/j.apcatb.2017.08.020>.
- [86] N.N. Lichtin, M. Sadeghi, Oxidative photocatalytic degradation of benzene vapor over TiO₂, *J. Photochem. Photobiol. Chem.* 113 (1998) 81–88. [https://doi.org/10.1016/S1010-6030\(97\)00327-4](https://doi.org/10.1016/S1010-6030(97)00327-4).
- [87] J. Coates, Interpretation of Infrared Spectra, A Practical Approach, in: *Encycl. Anal. Chem.*, John Wiley & Sons, Ltd, 2006. <https://doi.org/10.1002/9780470027318.a5606>.
- [88] M.E. Jenkin, J.C. Young, A.R. Rickard, The MCM v3.3.1 degradation scheme for isoprene, *Atmospheric Chem. Phys.* 15 (2015) 11433–11459. <https://doi.org/10.5194/acp-15-11433-2015>.